Contents lists available at ScienceDirect

Chemical Engineering Research and Design

journal homepage: www.elsevier.com/locate/cherd

Simulations of dissolution of spherical particles in laminar shear flow

J.J. Derksen[a,*], Gavin Reynolds[b], Alex Crampton[b], Zhenyu Huang[b], Jonathan Booth[b]

[a] School of Engineering, University of Aberdeen, Aberdeen AB24 3UE, Scotland, United Kingdom
[b] Pharmaceutical Development, AstraZeneca, Charter Way, Macclesfield SK10 2NA, United Kingdom

ABSTRACT

Simulations of dense suspensions of spherical solid particles in a Newtonian liquid carrier phase under simple shear flow have been performed. The simulations include solid–liquid mass transfer and (related) dissolution of the solids phase in the liquid. The interfaces between the solid particles and the liquid are fully resolved: in terms of the flow dynamics we apply a no-slip condition there and simulate the flow of the interstitial liquid by means of the lattice-Boltzmann method. In terms of mass transfer we solve a convection–diffusion equation for the solute concentration in the liquid with the saturation concentration imposed at the surface of the particles. The conditions are such that the flow is laminar (particle-bases Reynolds number significantly less than one). Peclet numbers are significant (order 100) which imposes strong demands on proper resolution of the mass transfer process. Results include dissolution times as a function of process conditions such as shear rate, solids loading, diffusivity and solubility.

Keywords: Dissolution; Solid–liquid suspension; Mass transfer; Lattice-Boltzmann; Solubility; Laminar shear flow

1. Introduction

Mass transfer between a solid phase and a liquid phase is at the heart of many engineered processes. Such processes operate at very diverse scales ranging from microns in microfluidic applications for e.g. medical diagnostics (Derveaux et al., 2008), to multiple meters in e.g. municipal wastewater treatment facilities. Transport phenomena in small-scale solid–liquid systems have our particular interest. Such systems often relate to the production of fine-chemicals and pharmaceuticals, and the details of the production process have a direct impact on product quality, process efficiency, and therefore on economic viability. Highly resolved numerical simulations are a way of revealing the complex physical interactions between the solids and the liquid phase which eventually determine mass transfer and product homogeneity. For example, the flow dynamics control mass transfer rates; mass transfer evolves the particle size distribution and generally results in an inhomogeneous solute distributions in the liquid phase that – in turn – may have impact on the flow dynamics, e.g. through local variations in the rheology of the solid–liquid mixture.

The process that was the direct motivation for the current numerical study is hot melt extrusion. Hot melt extrusion (HME) is considered a promising technique for dispersing poorly water-soluble drugs in a polymer matrix (Bikiaris, 2011a,b). In HME, particulate solid polymer and drug material are physically mixed and subsequently fed into an extruder. The shear imposed on the mixture by the extruder and external heating melt the polymer and dissolves and mixes the drug. After leaving the extruder through a die, the mixture is cooled and the end-product is a drug (in amorphous or crystalline form) dispersed in a polymer matrix. An important design objective of an HME process is uniformity of the final product, i.e. homogeneity of the drug/polymer mixture. This is not a trivial objective given the usually high viscosities of the polymer melt, finite solubility of the drug, and slow diffusion of the drug in the matrix. High viscosities imply a laminar

* Corresponding author.
E-mail addresses: jderksen@abdn.ac.uk, jos@ualberta.ca (J.J. Derksen).

Available online 5 July 2014
http://dx.doi.org/10.1016/j.cherd.2014.06.027

flow which has poor mixing capabilities. Product uniformity competes with constraints on process time due to potential decomposition of drug material when exposed to high temperature for prolonged time (Bikiaris, 2011b; Lakshman et al., 2009). HME has been studied mainly through experimentation where product properties are determined as a function of process conditions (e.g. Yang et al., 2010; Jijun et al., 2010). Visualization of the process itself is hindered by limits on optical accessibility due to the complex geometry of the internals of the extruder and non-transparent compounds. Numerical simulations, in principle, allow for a detailed look inside the process. Such simulations are the subject of the current paper where we focus on the interactions between drug particles suspended in a matrix and undergoing shear flow.

We anticipate interactions between drug particles to be important for two reasons. In the first place the particles will feel one another through mass transfer. The driving force for solid-to-liquid mass transfer is the difference between the solute concentration at the solid–liquid surface (the equilibrium concentration) and a far-field concentration. With many particles in the vicinity of a reference particle (which is the situation in a dense suspension) the far-field concentration increases, decreasing the driving force for mass transfer and thus dissolution of the reference particle. In the second place, particle-particle hydrodynamic interactions create a complex flow of the interstitial liquid which could positively influences mixing of solute.

In many papers, solid–liquid mass transfer is modeled through (Sherwood) correlations (Luan et al., 2013; Jones et al., 2012; Hartmann et al., 2006b). These usually have been measured/derived for single, isolated, spherical particles (Ranz and Marshall, 1952; Whitaker, 1972; Bird et al., 2006). Given our desire to study interactions between particles (in a mass transfer sense, as well as in a flow sense) we need a more detailed approach: we directly solve the convection–diffusion equation governing the scalar (solute) concentration in the liquid and use the equilibrium concentration as a boundary condition on the particle surfaces. Such a direct approach has also been applied (for a single sphere) recently by (Yang et al., 2011) and we use their results to benchmark our approach.

In recent years we have developed a simulation procedure for direct simulation of the flow of dense solid–liquid suspensions with full resolution of the solid–liquid interfaces (Ten Cate et al., 2004; Derksen and Sundaresan, 2007). This procedure we apply for representing the flow dynamics. An extension of the procedure is that the size of individual spheres is now a variable that we update in time according to the amount of solid mass that is transferred to the liquid.

In summary, the liquid and solids phase are coupled in multiple ways. In a hydrodynamic sense the liquid flow moves (translates and rotates) the particles and vice versa, the coupling principle being the no-slip condition at the solid surfaces. The liquid phase contains the solute that has dissolved from the solids phase and is convected by the liquid flow. The solute transport influences the flow dynamics through the particle sizes that evolve as a result of local solid-to-liquid mass transfer.

The aim of this paper is to propose a strategy for fully resolved, three-dimensional and time dependent simulations of dense solid–liquid suspension flow, including solid-to-liquid mass transfer (i.e. dissolution), and including particle sizes that evolve as a result of dissolution. The solid–liquid mixture undergoes simple shear as a rudimentary model for the deformations brought about by extrusion, as in HME. The key outcomes of this study are dissolution times as a function of process conditions and material properties.

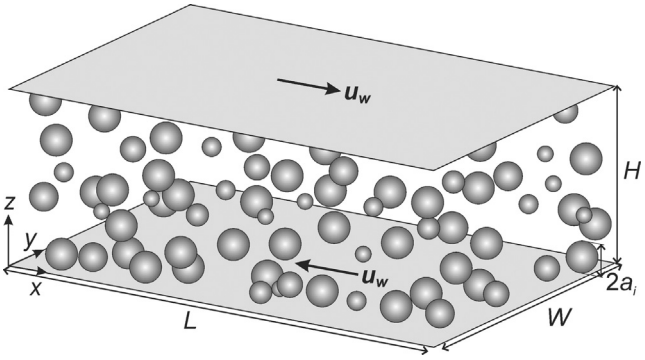

Fig. 1 – Flow geometry and coordinate system; a solid–liquid suspension is subjected to a shear rate $\dot{\gamma} = (2u_w/H)$ by moving two parallel plates in opposite direction. The solid particles are spheres with sphere number i having radius a_i.

This paper is organized in the following manner: we first define the flow systems that have been investigated. We do this in terms of a set of dimensionless numbers, part of which has been set to fixed values, part of which have been varied. Also the assumptions and simplifications to make the simulations tractable are discussed in detail here. Then we discuss the computational methods used, with references to our earlier works. In Section 5 we start with a number of qualitative observations on the dissolution process and the way the solute mixes with the liquid phase. We then show how the evolution of the dissolution process, and the dissolution time depends on process conditions. To place the simulation results into context, we compare the numerical results with those of a simple, semi-analytical model. In the final section we reiterate the conclusions.

2. Definition of the flow systems

Since in the HME process volume fractions of drug material are significant (order 0.3) we expect interactions between drug particles to play a significant role in the process and the simulations have been designed to assess particle interaction effects. At the same time a number of simplifying assumptions have been made in the simulations. Most importantly, we assume a sequence in melting of polymer and dissolution of the drug: first melting, then dissolution. This implies that we start our simulations with solid drug particles dispersed in a continuous phase liquid that represents the polymer melt. The liquid phase is assumed to be Newtonian and the particles are assumed to be spherical and stay spherical during the dissolution process. The flow imposed on this solid–liquid suspension is a simple shear flow. Given the constant overall shear rate, a constant viscosity assumption – i.e. Newtonian liquid – is a fair one.

2.1. *Flow dynamics*

A sketch of the typical flow system (including a Cartesian coordinate system) is given in Fig. 1. The solid–liquid suspension is confined between two, flat, parallel plates that move in opposite direction with velocity u_w thereby creating an overall shear rate $\dot{\gamma} = 2u_w/H$ with H the distance between the plates. The boundary conditions in x and y-direction are periodic, which

e.g. means that liquid or solid leaving at $x=L$ re-enters the flow domain at $x=0$ (and vice versa). The solid particles are assumed to be of spherical shape, and they stay spherical during the dissolution process. The radius of each individual particle is a function of time, i.e. $a^{(i)}(t)$ with i the number of the particle ($i=1\ldots N$ and N the total number of particles). At the start of each simulation all particles have the same radius $a^{(i)}(t=0)=a_0$, $i=1\ldots N$. These uniformly sized spheres are randomly placed in the flow domain. Initially liquid and spheres have zero velocity. We then switch on the shearing motion of the plates and first develop the flow without mass transfer (and thus without dissolution). Once the shear flow of the solid–liquid suspension is fully developed, mass transfer and dissolution are switched on. This moment we mark as $t=0$. The dissolution process is followed in time.

The density of the liquid and solids phase are identified as ρ and ρ_s respectively. The liquid is considered to be Newtonian with uniform kinematic viscosity ν, i.e. the liquid's viscosity (and also its density) does not depend on the (local) solute concentration and deformation rate. Given the high viscosities, the small particle sizes, and the small density differences between liquid and solid, settling of particles due to gravity is not considered important and gravity effects will be discarded.

Given the above, the three dimensionless input parameters that govern the flow dynamics at the start of the dissolution process are a Reynolds number that we define as $Re_0 \equiv (\dot{\gamma}a_0^2/\nu)$, the solids volume fraction at the start of a simulation: $\phi_0 \equiv (4\pi N a_0^3/3HLW)$, and the density ratio ρ_s/ρ. For ϕ_0 a typical value is 0.30; in this paper we will consider the range $0.20 \le \phi_0 \le 0.40$. As we will see in Section 4, the Reynolds number Re_0 based on initial sphere radius is of the order 10^{-6}, and Reynolds numbers based on e.g. channel height do not exceed 10^{-5}. This indicates creeping flow conditions. The density ratio is close to one; it has been fixed to $\rho_s/\rho = 1.25$. This implies that next to weak fluid inertia (low Re) also the inertia of the solids plays a minor role.

The finite size of the flow domain adds a number of aspects ratios to the set of dimensionless numbers: H/a_0, L/H, and W/H the effect of which will be examined in Section 5. The simulation procedure allows for particle collisions (with other particles or the bounding plates) to occur and a restitution and friction coefficient have been set to $e=1.0$ and $\mu=0.1$ respectively (the collision model we used is due to Yamamoto et al., 2001). However, given the high viscosity and a solid over liquid density ratio close to one, collisions are rare and effects of the collision parameters marginal.

2.2. *Mass transfer and dissolution*

We now turn to the mass transfer conditions relevant for the dissolution process. The solubility of the solids compound in the liquid phase has been characterized by the concentration ξ^e of that compound in the liquid in equilibrium with the solid. In transport phenomena terms the above means that the local and time dependent solute concentration in the liquid phase $\xi(\mathbf{x}, t)$ has $\xi=\xi^e$ as its boundary condition at the surface of the solids. The concentration field is governed by a convection–diffusion equation

$$\frac{\partial \xi}{\partial t} + \mathbf{u}\cdot\nabla\xi = \Gamma\nabla^2\xi \tag{1}$$

with $\mathbf{u}$ the liquid velocity field and Γ the diffusion coefficient. The latter parameter gives rise to a Peclet number: $Pe_0 \equiv \dot{\gamma}a_0^2/\Gamma$. At the surface of the two bounding walls the boundary condition $\partial\xi/\partial z=0$ applies. As was the case for the flow, the other boundaries are periodic.

The solid-to-liquid mass flux, and thus the dissolution rate, is governed by the (outward normal) concentration gradient at the surface of the particles: $\phi_m'' = -\Gamma\left.\frac{\partial\xi}{\partial n}\right|_{ss}$ with ϕ_m'' the mass flux (mass per unit area and unit time dissolving). The index ss indicates the location at the solid surface. In this research we assume that the solid particles stay spherical during the dissolution process. To determine the evolution of the radius of each particle in time the rate at which the particle is loosing mass is found by integration of the mass flux over the surface of the particle. The size reduction (of particle i) as a result of dissolution then obeys the following equation:

$$\frac{d}{dt}\left(\rho_s\frac{4\pi}{3}\left(a^{(i)}\right)^3\right) = -\int_{A^{(i)}}\phi_m''\,dA \tag{2}$$

with the integration over the surface $A^{(i)}$ of particle i.

Rather than working in terms of solute concentration ξ we will be working in terms of the concentration relative to the equilibrium concentration: $c \equiv (\xi/\xi^e)$ (which makes that $c=1$ at the solid particle surfaces). With this definition and some algebra we can rewrite Eq. (2) as

$$\frac{da^{(i)}}{dt} = \frac{\Gamma}{4\pi\left(a^{(i)}\right)^2}S\int_{A^{(i)}}\frac{\partial c}{\partial n}\,dA \tag{3}$$

where we have introduced the symbol $S \equiv (\xi^e/\rho_s)$ for solubility.

3. Numerical approach

3.1. *Suspension flow dynamics*

We used the lattice-Boltzmann (LB) method (Chen and Doolen, 1998; Succi, 2001) to solve the liquid flow. The specific scheme employed is due to Somers (1993); also see Eggels and Somers (1995). The method has a uniform, cubic grid (grid spacing Δ), is fully three-dimensional and time-dependent.

The no-slip boundary conditions at the moving upper and lower wall were implemented according to the half-way bounce-back rule (Succi, 2001). The no-slip conditions at the particles' surfaces were dealt with by means of an immersed boundary (or forcing) method (Derksen and Van den Akker, 1999; Ten Cate et al., 2002). In this method, the solid surfaces are defined as sets of closely spaced points (the typical spacing between points is 0.7Δ), not coinciding with lattice points. At these points the (interpolated) fluid velocity is forced to the local velocity of the solid surface according to a control algorithm. The local particle surface velocity has contributions from translational and rotational motion of the sphere under consideration. Adding up (discrete integration) per spherical particle of the forces needed to maintain no-slip provides us with the (opposite; action equals minus reaction) force the fluid exerts on the spherical particle. Similarly the hydrodynamic torque exerted on the particles can be determined. Forces and torques are subsequently used to update the linear and rotational equations of motion of each spherical particle. This update determines the new locations and velocity of the sphere surface points that are then used to update the liquid flow, and so forth.

The spheres directly interact through hard-sphere collisions according to the two-parameter model (restitution

coefficient e and friction coefficient μ) due to Yamamoto et al. (2001). The same e and μ were also used when a sphere hits one of the bounding walls. The restitution coefficient was set to $e=1$ and the friction coefficient to $\mu=0.1$ (Derksen, 2011b) throughout this work.

Fixed-grid simulations involving moderately dense suspensions as discussed here require explicit inclusion of sub-grid lubrication forces (Nguyen and Ladd, 2002): if the surfaces of two spherical particles get closer than (typically) the grid spacing Δ, the flow solver is not able to resolve the flow in between the surfaces anymore. At this stage the interaction forces (termed lubrication forces) can get significant and need to be accounted for. For creeping flow in between closely spaced spheres, the expression for the radial lubrication force on two solid spheres i and j with center locations $\mathbf{x}_{pi}$ and $\mathbf{x}_{pj}$, radii $a^{(i)}$ and $a^{(j)}$, having relative velocity $\Delta\mathbf{u}_{ij}\equiv\mathbf{u}_{pj}-\mathbf{u}_{pi}$ reads (Kim and Karrila, 1991)

$$F_{lub}=6\pi\rho\nu\frac{(a^{(i)}a^{(j)})^2}{(a^{(i)}+a^{(j)})^2}\frac{1}{s}(\mathbf{n}\cdot\Delta\mathbf{u}_{ij}),\quad \mathbf{F}_{lub,j}=-F_{lub}\mathbf{n},\quad \mathbf{F}_{lub,i}=F_{lub}\mathbf{n} \tag{4}$$

with s the smallest distance between the sphere surfaces $s\equiv\left|\mathbf{x}_{pj}-\mathbf{x}_{pi}\right|-(a^{(i)}+a^{(j)})$, and $\mathbf{n}$ the unit vector pointing from the center of sphere i to the center of sphere j. The lubrication force on one sphere (say sphere i) in the vicinity of a plane wall follows from Eq. (4) by taking the limit $a^{(j)}\to\infty$ and setting $u_{pj,z}=0$. As noted above, Eq. (4) is for creeping flow in the narrow gap between closely spaced spheres undergoing relative motion and thus is valid if $Re_s\equiv(s\left|\Delta\mathbf{u}_{ij}\right|/\nu)\ll 1$, which is a condition that is satisfied here. Tangential lubrication forces and torques have not been considered since they generally are much weaker than the radial lubrication force; the former scale with $\ln(a^{(i)}/s)$ (Kim and Karrila, 1991), the latter (see Eq. (4)) with $(a^{(i)}/s)$.

The expression in Eq. (4) has been tailored for use in lattice-Boltzmann simulations according to (Derksen and Sundaresan, 2007; Nguyen and Ladd, 2002): (1) the lubrication force needs to be switched off when surfaces are sufficiently far apart in which case the grid associated with the LB method can accurately account for the hydrodynamic interaction between the spheres (typically if $s>\Delta$). (2) The lubrication force needs to saturate when solid surfaces are very close to account for surface roughness and to avoid very high levels of the lubrication force that could lead to unphysical instabilities in the simulations. To achieve Objective (1) instead of Eq. (4) one writes

$$F_{lub}=6\pi\rho\nu\frac{(a^{(i)}a^{(j)})^2}{(a^{(i)}+a^{(j)})^2}\left(\frac{1}{s}-\frac{1}{s_a}\right)(\mathbf{n}\cdot\Delta\mathbf{u}_{ij})\quad\text{if}\quad s\le s_a,\quad\text{and}$$
$$F_{lub}=0\quad\text{if}\quad s>s_a \tag{5}$$

with the modeling parameter s_a the distance between solid surfaces below which the lubrication force becomes active. For Objective (2) a second modeling parameter s_b is introduced as the distance below which the lubrication force gets saturated: $F_{lub}=6\pi\rho\nu\frac{(a^{(i)}a^{(j)})^2}{(a^{(i)}+a^{(j)})^2}\left(\frac{1}{s_b}-\frac{1}{s_a}\right)(\mathbf{n}\cdot\Delta\mathbf{u}_{ij})$ if $s\le s_b$. The settings for s_a and s_b were $s_a=0.2a_0$ and $s_b=2\times10^{-4}a_0$. With this procedure and these settings accurate results for close-range hydrodynamic sphere-sphere interactions have been achieved (Derksen and Sundaresan, 2007).

The spheres' equations of linear and rotational motion including resolved and unresolved (i.e. lubrication) forces are integrated according to an explicit split-derivative method (Feng and Michaelides, 2009; Shardt and Derksen, 2012). These time-step driven updates are linked with an event-driven algorithm that detects and carries out hard-sphere collisions and sphere-wall collisions during the time steps. Once an event is being detected, all particles are frozen and the event is carried out which implies an update of the linear and angular velocities of the sphere(s) involved in the event. Subsequently all spheres continue moving until the end of the time step, or until the next event, whatever comes first. The hard-sphere algorithm has been verified by carrying out granular simulations (no interstitial fluid). Zero-overlap of sphere volumes, and exact energy conservation (if $e=1$ and $\mu=0$) have been confirmed (Derksen, 2011a).

3.2. Scalar transport and dissolution

We solve the scalar transport equation (Eq. (1)) with an explicit finite volume discretization. Away from the spherical particles we use the same (uniform and cubic) grid as the LBM. A clear advantage of employing a finite volume formulation is the availability of methods for suppressing numerical diffusion. As in previous works (Hartmann et al., 2006a; Derksen, 2008a), TVD discretization with the Superbee flux limiter for the convective fluxes (Sweby, 1984; Wang and Hutter, 2001) was employed. We step in time according to an Euler explicit scheme with the same time step as used by the LBM.

Given the low diffusivity of the scalar concentration in the liquid phase (or better: given that Peclet numbers are significantly larger than one), and given the $c=1$ boundary condition at the solid particle surfaces we expect thin concentration boundary layers there that are hard to resolve on the cubic grid. Resolution of these boundary layers is very important since they largely determine the solid–liquid mass transfer and thus the dissolution rate. Applying a very fine grid for resolving the scalar transport throughout the entire flow domain is computationally unfeasible (and also not necessary). Instead, we equip each particle with a spherical grid in a shell around the particle, see Fig. 2. This grid is very fine in the radial direction and coarser in the two angular directions; it moves with the particle over the fixed cubic grid. The thickness of the shell is $\delta=0.2a_0$. The concentration fields in the inner (spherical) and outer (cubic) grid are matched at the edge of the spherical shell through linear interpolation of concentrations. A finite volume method has also been used to discretize Eq. (1) on the spherical grids. Given the small grid spacing in radial direction, and the explicit time stepping in this direction, the finite volume time step on the spherical grid is much smaller than the LBM time step, i.e. during each LBM time step the spherical solution goes through a number (typically 8–16) of sub time steps.

We have taken a fairly crude and simple approach for situations in which the distance between sphere surfaces gets smaller than 2δ. Then the concentration shells around the spheres overlap. We do *not* directly consider this overlap when solving the transport equations in each spherical grid. The overlap is directly felt by the cubic grid in the sense that the two spherical grids that (in case of overlap) contribute to the concentration in a cubic grid node get the average concentration from the two spherical grids. Since in the next time step the cubic grid concentrations are fed back to the spherical grids as boundary conditions, also the

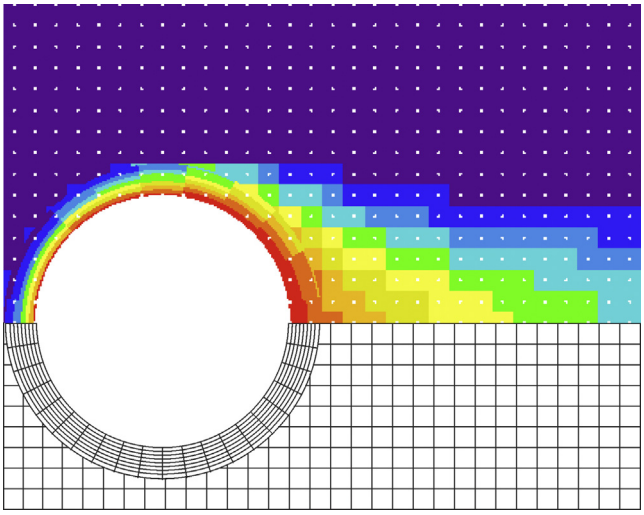

Fig. 2 – Illustration of the dual grid used for mass transfer calculations. The spherical grid moves with the sphere; the cubic "far-field" grid is fixed. The two grids are connected through boundary conditions: the (interpolated) concentrations on the two grids are matched on the outer shell of the spherical grid.

spherical grids (indirectly) sense their overlap. By making the shells as thin as possible we somewhat mitigate overlap issues. Improving the numerical procedure toward a direct interaction between the spherical grids is left for future work.

3.3. *Spatial and temporal resolution*

In this work, the default spatial resolution of the LB simulations has been set such that the initial sphere radius a_0 spans 8 lattice spacings ($a_0 = 8\Delta$); if the initial radius of the spheres is 100 μm, then one lattice spacing thus represents 12.5 μm. The spatial resolution of the outer (cubic) finite volume simulations is the same. The spherical grids around the particles have spacings in radial direction of typically $\Delta r = 0.1\Delta$ (and thus $\Delta r = a_0/80$). In the two angular directions the grid is much coarser: $\Delta\theta = \Delta\varphi = \pi/10$ which makes the grid spacings at the surface of the sphere in these directions equal to $a_0\Delta\theta = a_0\Delta\varphi \approx 2.5\Delta$. The fine grid in the r-direction and the explicit approach to solving the concentration field around the sphere makes the time step on the spherical grid one order of magnitude smaller than on the cubic grid.

The LB and cubic grid time step in the simulations can be related to physical time via the shear rate $\dot{\gamma}$. If we (as an example) suppose that in the physical system $\dot{\gamma} = 10\,\mathrm{s}^{-1}$, then a time span of $t = 1$ s has dimensionless time $\dot{\gamma}t = 10$. In a typical simulation the distance between the plates H spans 77 lattice spacings, while the plates have a velocity $u_w = 0.025$ (lattice spacings per time step) so that $\dot{\gamma} = 2u_w/H \approx 6.5 \times 10^{-4}$ (in lattice units). This means that we need $10/6.5 \times 10^{-4} \approx 1.5 \times 10^4$ time steps to simulate 1 s in real time in case $\dot{\gamma} = 10\,\mathrm{s}^{-1}$.

3.4. *Resolution requirements*

The suspension dynamics part of the numerical procedure has been verified and validated in a number of previous studies (Derksen and Sundaresan, 2007; Derksen, 2011a,b). Various solid–liquid systems were used for this: experimental validation through PIV experiments of a single settling sphere (Ten Cate et al., 2002), and verification through comparing simulation results with analytical solutions under creeping flow conditions (Derksen, 2008b; Derksen and Larsen, 2011). Dense fluidized solid–liquid suspensions (solids volume fractions up to 0.5) showed instabilities (planar waves and voids) in quantitative agreement with experimental work (Derksen and Sundaresan, 2007). Verifications and validations included assessment of the effect of grid resolution. They indicate that a spatial resolution such that a sphere radius spans four lattice spacings ($a = 4\Delta$) gives numerical results in good agreement with experimental data and analytical solutions up to a particle-based Reynolds number of 30 (Ten Cate et al., 2002). In this study the initial size of the spheres is $a_0 = 8\Delta$. We follow the dissolution process of a sphere until its radius is $a = 0.1a_0$ after which we consider it dissolved. Therefore, in the later stages of the dissolution process we tend to under-resolve the spheres. This is not considered a serious concern because in this study particle-based Reynolds and Stokes numbers are low which relaxes resolution requirements, and because once the spheres reach a potentially under-resolved state the suspension is not dense anymore which also relaxes resolution requirements: less dense suspensions need less resolution to resolve the flow of interstitial liquid given the wider spaces between the particles.

3.5. *Benchmarking*

The novel part of the numerical procedure relates to scalar transport and solid–liquid mass transfer; more specifically the dual grid approach to resolve the scalar boundary layers around the particles (see Fig. 2). This part of the computer code has been benchmarked by means of recent results due to Yang et al. (2011). They placed a single sphere in shear flow and numerically solved the flow (including the flow-induced rotation of the sphere) and mass transfer with a given and fixed concentration boundary condition at the surface of the sphere. Note that in this benchmark the sphere does not dissolve and the sphere thus has a time-independent radius a. In Fig. 3 we compare their results at Schmidt number $Sc \equiv (\nu/\Gamma) = 300$ (based on their Fig. 12, Yang et al., 2011) with results from our methodology obtained with the resolution given in the previous subsection ($a = 8\Delta$, $\Delta r = a/80$, $\Delta\theta = \Delta\varphi = \pi/10$), and the default spherical shell thickness of $\delta = 0.2a$. Fig. 3 shows the steady state Sherwood number Sh (same as Nu(sselt) in Yang et al., 2011) as a function of Pe. The Sherwood number is the dimensionless mass transfer coefficient: $Sh \equiv (\phi''_m a/\Gamma\xi^e)$ (note that the length scale is the sphere radius a, not the diameter $2a$; ξ^e is the concentration at the solid surface). We observe good agreement (deviations less than 5%) in the range $10 \le Pe \le 2000$ which is a slightly wider range than the range of initial Peclet numbers Pe_0 used in the dissolution simulations (see Table 1 in the next section). It was our experience that making the shell thinner than $\delta = 0.2a$ led to poorer Sherwood number predictions.

4. Summary of input parameters and dimensionless numbers

As a basis for the dissolution simulations we consider the following physical system: initial particle radius $a_0 = 100$ μm (i.e. diameter 200 μm); liquid kinematic viscosity $\nu = 0.2$ m^2/s; solid over liquid density ratio $(\rho_s/\rho) = 1.25$. For the initial solids volume fraction we consider the range $0.20 \le \phi_0 \le 0.40$; for the shear rate the range $1\,\mathrm{s}^{-1} \le \dot{\gamma} \le 100\,\mathrm{s}^{-1}$. In the physical system the solubility depends on the temperature. In the temperature

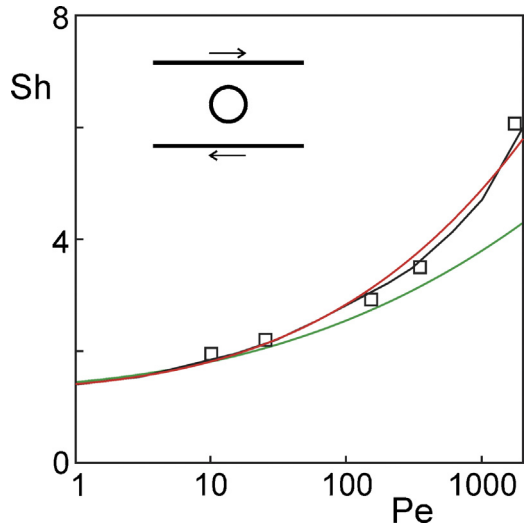

Fig. 3 – Sherwood number *Sh* based on (in this benchmark constant) sphere radius *a* as a function of the Peclet number $Pe = (\dot{\gamma}a^2/\Gamma)$ at $Sc = 300$ for mass transfer from a sphere in simple shear flow. Comparison between results due to Yang et al. (2011) (black curve) and the present work (open squares). The red curve is a fit according to Eq. (9). The green curve is a fit to Yang et al's data (not shown in this figure) for $Sc = 1000$.

range 180–200 °C we have $0.4 \leq S \leq 0.6$. The diffusivity of the solute in the carrier liquid is unknown. We therefore have simulated a range of diffusivities that are typical for diffusion in liquids: $10^{-9}\text{m}^2/\text{s} \leq \Gamma \leq 10^{-8}\text{m}^2/\text{s}$. The ranges in $\dot{\gamma}$ and in Γ generate a wide range in Peclet numbers ($Pe_0 \equiv (\dot{\gamma}a_0^2/\Gamma)$): $1 \leq Pe_0 \leq 10^3$ that has been largely (not fully though) covered in the simulations, see Table 1.

Table 1 summarizes the dimensionless system parameters, including their values or ranges. From a numerical point of view the Reynolds number and the upper part of the Peclet range are concerns. In order to reach Reynolds numbers as low as given in the table one would need to set a very high viscosity which would limit the accuracy of the lattice-Boltzmann method (Succi, 2001), or a very low u_w which would make the simulations unpractically lengthy (too many time steps would be needed). We realize, however, that once the Reynolds number is low (i.e. significantly smaller than one), the dynamics of the flow gets independent of Reynolds (Batchelor, 1967). This allows us to set Re_0 to the practical (and fixed) value of 0.05 and consider the flow with this value of Re_0 dynamically equivalent to flows with the Reynolds number given in Table 1.

Table 1 – Dimensionless input parameters defining the simulation cases and their settings.

Parameter	Description	Fixed	Range
ϕ_0	Initial solids volume fraction		0.2–0.4
Re_0	Initial particle Reynolds number based on shear rate and a_0	5×10^{-7} (**0.05**)	
ρ_s/ρ	Solid over liquid density ratio	1.25	
Pe_0	Initial Peclet number		20–800
S	Solubility		0.4–0.6
e	Restitution coefficient	1.0	
μ	Friction coefficient	0.1	
H/a_0	Gap width over initial particle radius	9.6	
L/H	Domain length over height	1.66	
L/W	Domain length over width	2	

Complete dissolution is only possible if the total mass of initial solid can be contained in the liquid, i.e. if $\rho_s\phi_0 < \xi^e$, in other words if $\phi_0 < S$. Since we aim for all the solids getting dissolved in the liquid, only situations where the latter condition is met have been studied.

5. Results

5.1. *Impressions of the flow and scalar fields*

Before starting the dissolution process, first the suspension shear flow with uniformly sized spheres of radius a_0 is developed toward a dynamically stationary state. In Fig. 4 we show the developed flow in different perspectives and for three different solids volume fractions. The periodic boundary conditions in streamwise (and also in spanwise) direction can be identified from the panels in the figure: if a sphere is cut-off at an edge, the rest of the same sphere shows up at the opposite side of the domain. Given the denseness of the suspensions most insight in the flow is obtained in a cross sectional view, less so from a (three-dimensional) side view and in the rest of this section we will be showing such cross sections (as in the middle row of Fig. 4).

After the flow is fully developed, mass transfer is switched on (at $t = 0$) and the solid spheres start to dissolve. For a specific combination of Peclet number and solubility ($Pe_0 = 200$ and $S = 0.6$) the dissolution process and the way it evolves in time is visualized for the three initial solids volume fractions ($\phi_0 = 0.2$, 0.3, and 0.4) considered in this paper in Fig. 5. The figure qualitatively shows that the higher solids loadings lead to a slower dissolution process. This is because the higher solids loadings give rise to higher solute concentrations in the liquid which reduces the difference in concentration between the solid surfaces (the equilibrium concentration) and the "bulk" liquid and thus reduces the driving force for solid–liquid mass transfer. For the case with $\phi_0 = 0.2$ the solids are fully dissolved after $\dot{\gamma}t = 100$. At this time, however, the solute has not uniformly mixed in the shear flow; the concentration at the walls is lower than in the middle of the channel; the system still "remembers" the solids fraction profile with lower solids volume fraction directly at the walls (wall exclusion effects). In this laminar flow, diffusion is the only mechanism to eventually even out the solute concentration gradients in the wall-normal direction.

In Fig. 6 we compare situations that all have an initial solids volume fraction of $\phi_0 = 0.3$. In the left column it shows that in terms of dimensionless time units $\dot{\gamma}t$ dissolution goes slower if we increase the Peclet number. This is easy to understand if we imagine to increase Pe_0 by decreasing the diffusion coefficient: with a reduced diffusion coefficient the mass flux at the solids surfaces reduces and thus the rate at which the spheres shrink (see Eq. (3)).

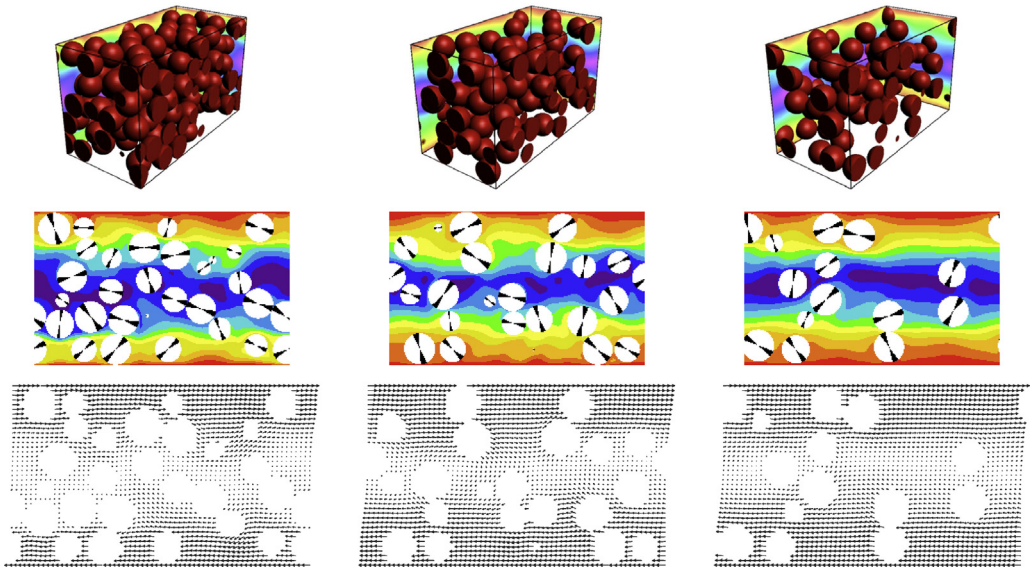

Fig. 4 – Instantaneous realizations of fully developed flow with uniformly sized spheres of radius a_0, i.e. before dissolution starts. From left to right $\phi_0 = 0.4$, 0.3, and 0.2 respectively. From top to bottom: three-dimensional view with the contour colors indicating liquid velocity magnitude; cross section with again colors indicating liquid velocity and the "whiskers" indicating the orientation of the spheres; liquid velocity vectors in the same cross section. $Re_0 = 0.05$ and $\rho_s/\rho = 1.25$.

The right column of Fig. 6 compares cases that only differ in terms of the solubility; from top to bottom the solubility increases ($S = 0.2$, 0.4, and 0.6 respectively). Comparing the three panels in this column demonstrates the full and intimate coupling between the three sub-processes that determine the overall dissolution process: flow dynamics, scalar transport in the liquid, and solid–liquid mass transfer. One observes that the concentrations in the liquid on average increase with decreasing solubility. It should be noted, however, that the concentrations in Fig. 6 are concentrations scaled with the equilibrium concentration ($c \equiv (\xi/\xi^e)$) so that the actual concentration (e.g. in kg/m^3) in the liquid decreases with decreasing solubility (as should be). This makes that spheres shrink slower at low solubility (as can be seen in the figure). We then do understand why the dimensionless concentrations are (on average) higher for lower S: for lower S the

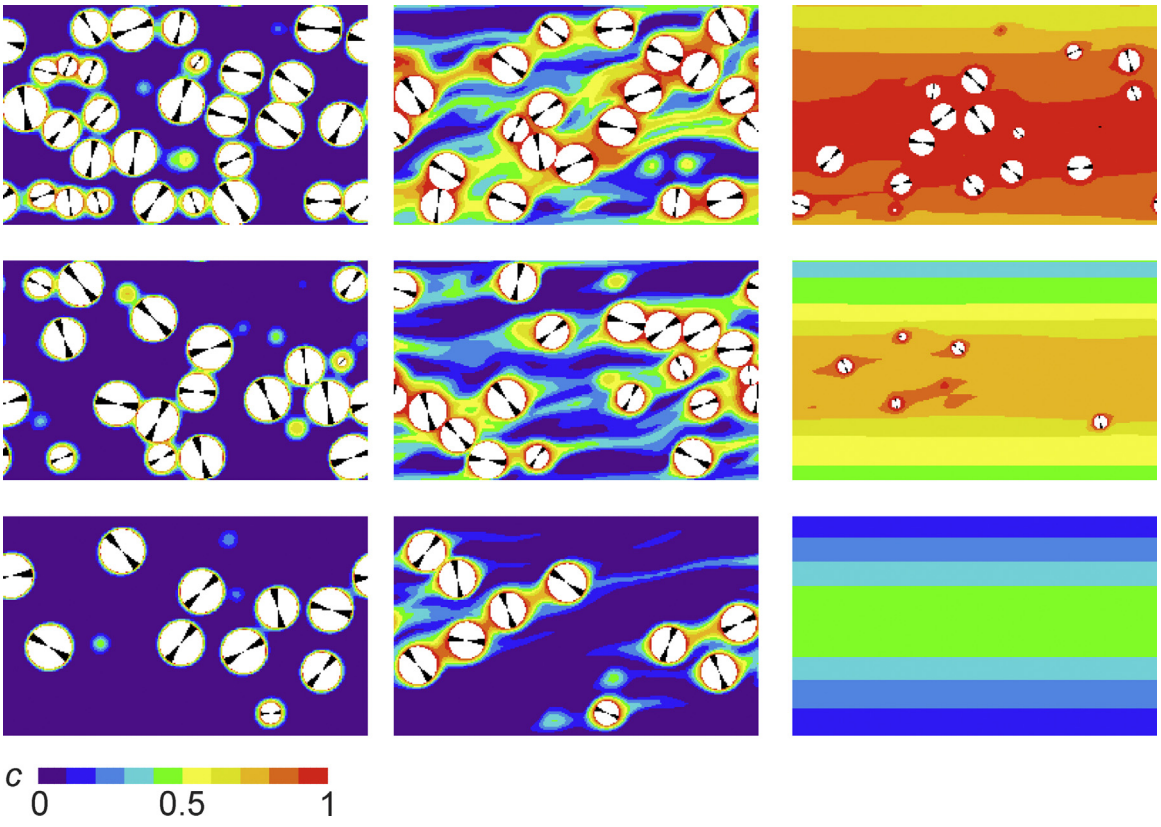

Fig. 5 – Instantaneous realizations of the concentration fields and the dissolving particles in a *xz*-cross section. From bottom to top $\phi_0 = 0.2$, 0.3, and 0.4. From left to right: $\dot{\gamma}t = 1$, 10, and 100. In all cases $Pe_0 = 200$ and $S = 0.6$.

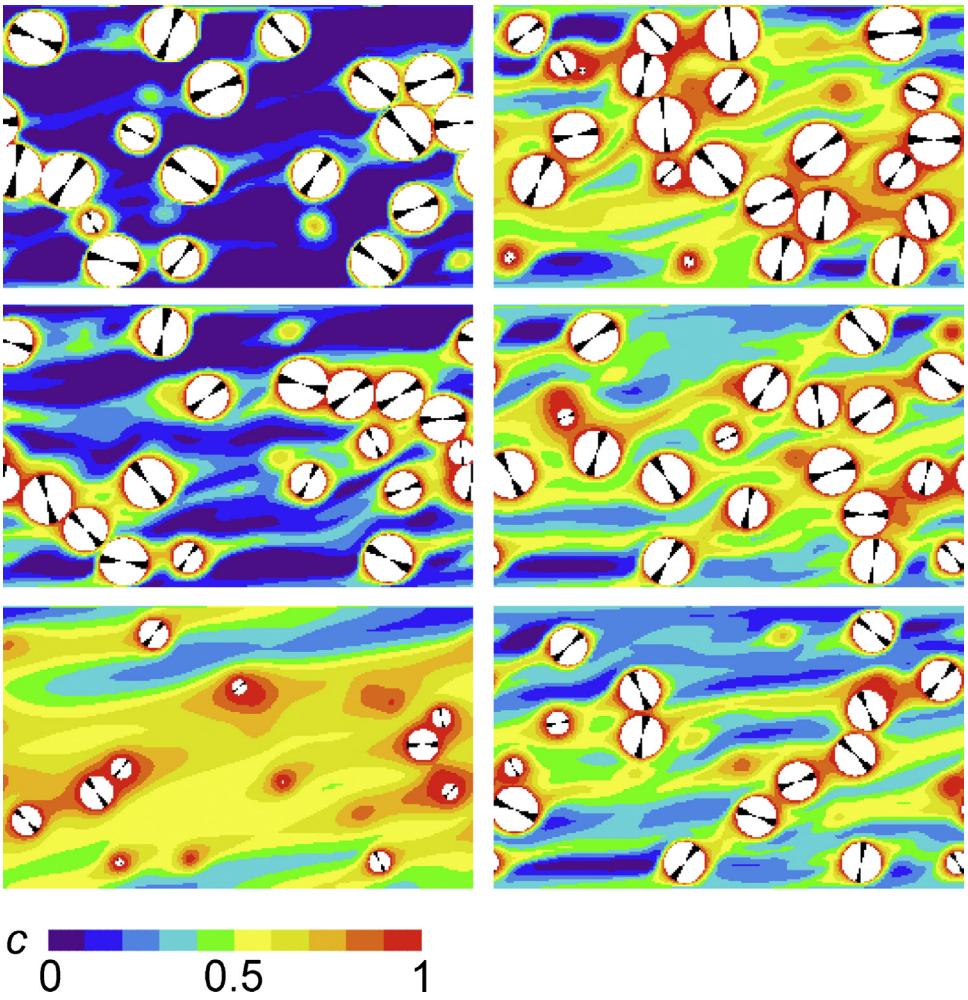

Fig. 6 – Instantaneous realizations of the concentration fields and the dissolving particles in a *xz*-cross section for simulations with $\phi_0 = 0.3$. Left column: influence of the initial Peclet number. From bottom to top $Pe_0 = 50$, 200, and 800. All three panels on the left have $S = 0.6$ and are at $\dot{\gamma}t = 10$. Right column: influence of solubility. From bottom to top $S = 0.6$, 0.4, and 0.2. All three panels on the right have initial Peclet number $Pe_0 = 200$ and are at $\dot{\gamma}t = 20$.

spheres are on average larger, and so is the solid–liquid interfacial area which enables more *scaled* (with ξ^e) mass transfer compared to higher S situations.

5.2. *Quantitative analysis*

The observations so far were qualitative. We now will look in a more quantitative sense at the simulation results. In the first place we will consider the way the solids volume fraction decays in time as a result of dissolution. This is shown in Fig. 7 where the three panels relate to the three different initial solids volume fractions ($\phi_0 = 0.2$, 0.3, and 0.4). The different curves per panel are for different initial Peclet numbers Pe_0. All data in Fig. 7 are at $S = 0.6$. The overall trends are that cases with higher Peclet numbers have longer dimensionless dissolution times, and that higher initial solids volume fractions take longer to dissolve.

All curves show a very fast initial decay. This is when solute penetrates the fresh liquid around the solid surfaces with initially very high concentration gradients – and thus diffusive mass fluxes – at the solid surfaces. This is a highly unsteady diffusion process with high but quickly decaying mass transfer coefficients. After this, the decay of ϕ slows down, most strongly so for $\phi_0 = 0.4$. At the later stages the solute concentration in the liquid gets significant which reduces the concentration difference between solid surfaces and bulk liquid and thus the driving force for solid–liquid mass transfer.

Most of the simulations presented have a domain size $H \times L \times W$ as specified in Table 1. To check if this domain is large enough we compare in Fig. 8 dissolution results in the default domain with results obtained in larger domains (and further the same conditions). An increased domain size in the streamwise and lateral direction has no noticeable effect on the dissolution process. If the domain is increased in wall-normal direction the dissolution is slightly faster (the dissolution time – precisely defined below – reduces by less than 5%). This is due to the fact that the wall regions are less effective in mass transfer (see e.g. Fig. 5, lower-right panel), and narrower domains have relatively larger wall regions.

We do not want to quantify dissolution time with the moment when ϕ becomes zero as this would depend too much on the fairly random circumstances of the final (few) undissolved particles. Instead we use the moment when 95% of the solids has dissolved (i.e. $t\dot{\gamma} = t_{95}\dot{\gamma}$ when $\phi = 0.05\phi_0$) as a metric for dissolution time. This dissolution time as a function of the initial Peclet number Pe_0 is presented in Fig. 9. It shows close to linear relationships. In practical terms this implies two things: (1) the dissolution time is very sensitive to the diffusion coefficient. (2) Increasing the shear rate does not help in reducing

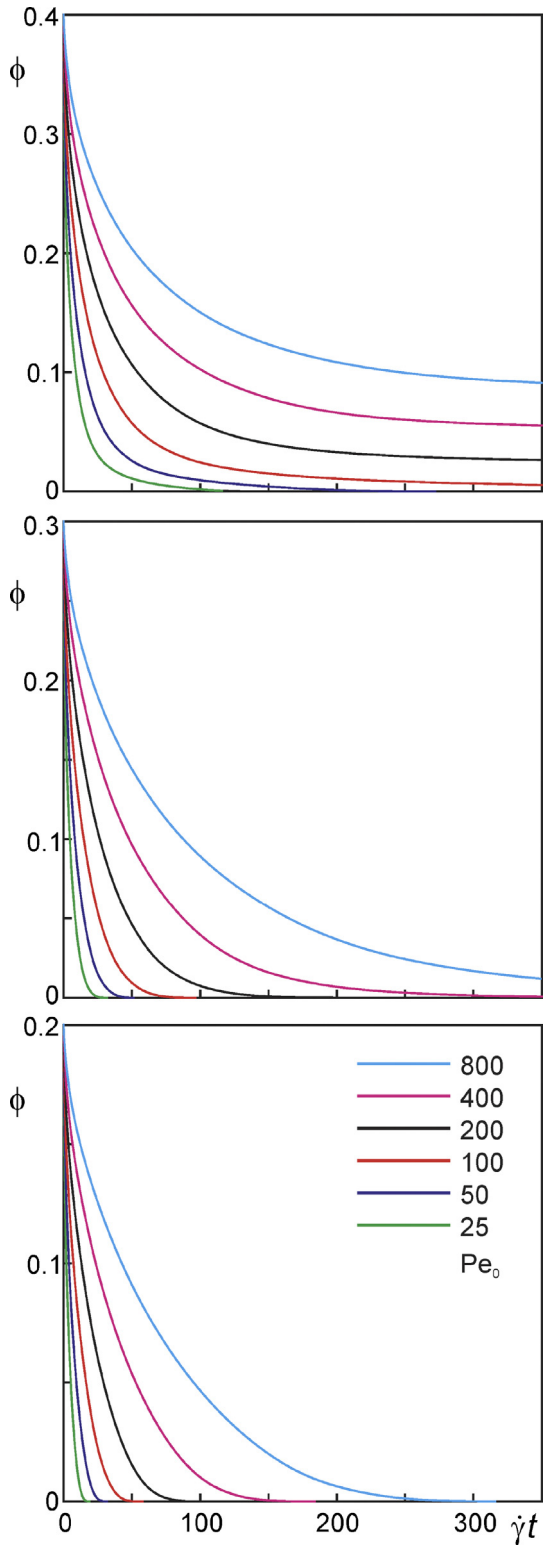

Fig. 7 – Decay of the solids volume fraction (ϕ) as a function of time as a result of dissolution. From top to bottom: $\phi_0 = 0.4$, 0.3, and 0.2. The line colors indicate the initial Peclet number Pe_0. The solubility is $S = 0.6$.

the real (dimensional) dissolution time: if we double $\dot{\gamma}$, we double Pe_0. Fig. 9 then implies that we also double $t_{95}\dot{\gamma}$ so that t_{95} does not get smaller.

During the dissolution process, each particle feels a different hydrodynamic and concentration environment due to the random nature of the suspension. How this translates in particle size distributions is shown in Fig. 10. These size distributions are averages over at time interval δt as specified in the

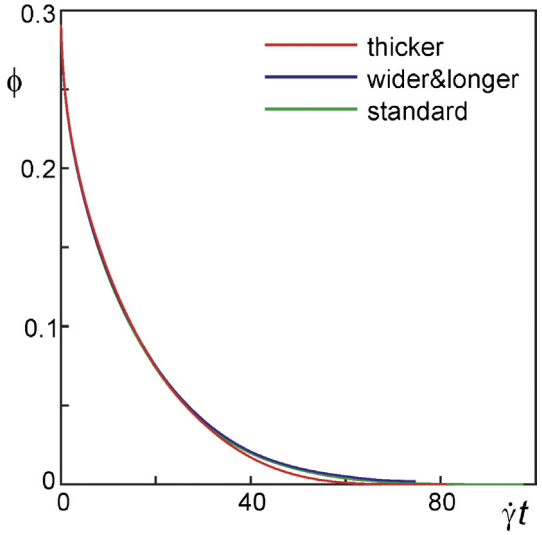

Fig. 8 – Effect of the domain size on the dissolution process; "standard" indicates the default domain (see Table 1), "wider & longer" is a domain stretched 1.5 times in x and y-direction, "thicker" is a domain stretched by a factor of 1.5 in z-direction. $\phi_0 = 0.3$, $Pe_0 = 100$, $S = 0.6$.

caption of Fig. 10. During this time at least 20 single realizations of the full particle population were taken and particles were sorted in bins with a width of $0.02a_0$.

Starting from a monodisperse system there is an evolution toward a wider size distribution. The higher the solids volume fraction, the wider the distribution gets for later times; clearly particles in a dense suspension see a more heterogeneous environment than particles in a more dilute suspension.

Results so far were for a solubility of $S = 0.6$. Simulations were also conducted for $S = 0.4$ (only for $\phi_0 = 0.2$ and 0.3 as these cases satisfy the full dissolution criterion $\phi_0 < S$). Reduction of S strongly slows down the dissolution process as shown in Fig. 11. Typically $t_{95}\dot{\gamma}$ slows down by a factor of 2 for $\phi_0 = 0.2$, and a factor of 5–7 for $\phi_0 = 0.3$. The linearity between Pe_0 and $t_{95}\dot{\gamma}$ is retained for lower S.

6. A semi-analytical model for dissolution

For further interpretation of the dissolution results a simple model for the dissolution process has been built. The model has been written in the form of an ordinary differential equation (ODE) in the solids volume fraction as a function of time. This ODE can easily and quickly be solved numerically. The main assumptions in the model are (1) a known relation for the Sherwood number as a function of the Peclet number to describe the mass transfer between spheres in shear flow and the surrounding liquid; (2) no interaction (in terms of hydrodynamics and in terms of scalar transport) between the spheres in the suspension (this implies that all spheres see the same environment and shrink at the same rate); (3) a uniform (i.e. well-mixed) "bulk" concentration in the liquid, away from the particles. By comparing the simulations with the simple-model-results we are able to assess to what extent non-idealities such as particle-particle interactions influence the dissolution process.

With the assumptions given above, a solids mass balance for N non-interacting spheres suspended in a volume V reads

$$\frac{d}{dt}(\rho_s \phi V) = -Sh\frac{\Gamma}{a}N4\pi a^2(\xi^e - \xi^b) \tag{6}$$

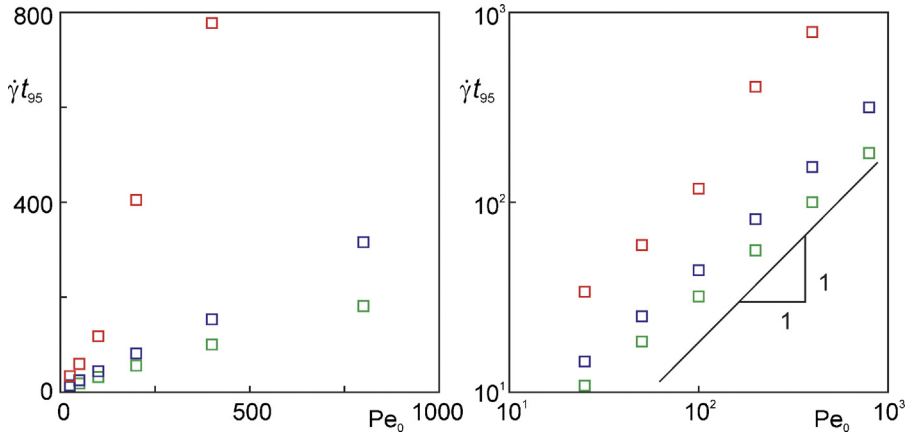

Fig. 9 – Time to 95% dissolution t_{95} as a function of the initial Peclet number Pe_0 for $\phi_0 = 0.2$ (green), 0.3 (blue), and 0.4 (red). $S = 0.6$. Left: linear scale; right (to highlight the lower left corner in the left panel): logarithmic scale.

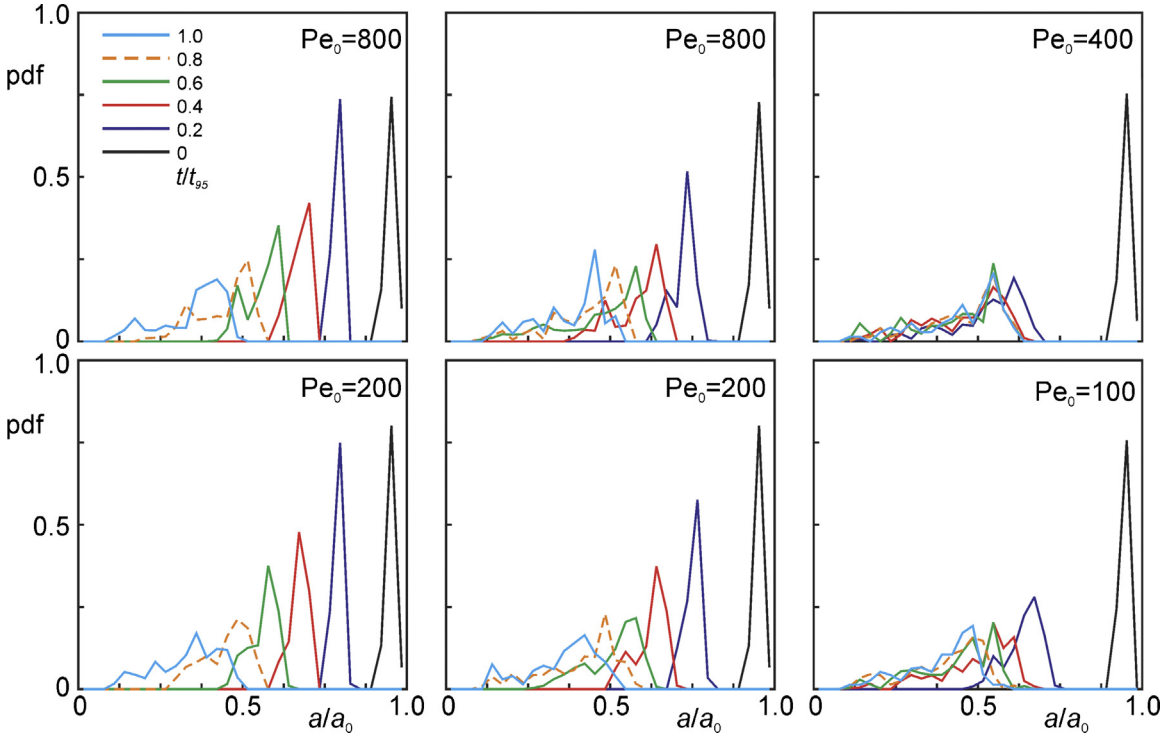

Fig. 10 – Particle size distributions as they evolve in time. Left column $\phi_0 = 0.2$; middle column $\phi_0 = 0.3$; right column $\phi_0 = 0.4$. Initial Peclet numbers as indicated. All cases shown have $S = 0.6$. The moments in time given are fractions of t_{95}. Each particle size distribution is the average over a certain time range δt. For cases with $Pe_0 = 200$ this was $\delta t = (1/\dot{\gamma})$; for $Pe_0 = 800$ it was $\delta t = (4/\dot{\gamma})$; for $Pe_0 = 100$ it was $\delta t = (0.5/\dot{\gamma})$; for $Pe_0 = 400$ it was $\delta t = (2/\dot{\gamma})$.

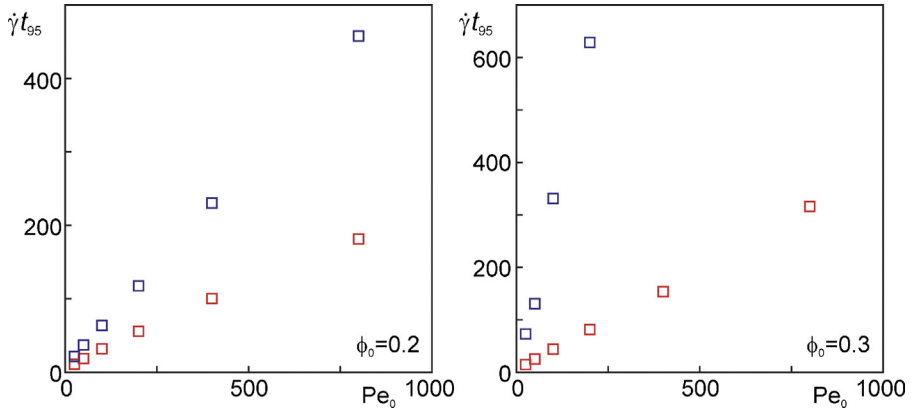

Fig. 11 – Dissolution time as a function of Pe_0. Comparison between $S = 0.6$ (red) and $S = 0.4$ (blue). Left: $\phi_0 = 0.2$; right: $\phi_0 = 0.3$.

with Sh a function of $Pe = (\dot{\gamma}a^2/\Gamma)$ and Pe a function of time since a is a function of time. The driving force for mass transfer is the difference between the equilibrium concentration and the bulk concentration $\xi^e - \xi^b$. The bulk concentration is the amount of solid material that has dissolved divided by the liquid volume: $\xi^b = \rho_s(V(\phi_0 - \phi)/(1-\phi)V)$. If we substitute the latter expression in Eq. (6) and rearrange we get

$$\frac{d}{dt}(\phi) = -Sh\frac{\Gamma}{a}\frac{N}{V}4\pi a^2\left(S - \frac{(\phi_0 - \phi)}{(1-\phi)}\right) \tag{7}$$

Instead of in real time we write this equation in dimensionless time $\dot{\gamma}t$. This introduces the Peclet number based on the initial particle radius ($Pe_0 \equiv (\dot{\gamma}a_0^2/\Gamma)$) in the mass balance:

$$\frac{d}{d(\dot{\gamma}t)}(\phi) = -\frac{Sh}{Pe_0}\frac{N}{V}4\pi a_0^2 a\left(S - \frac{(\phi_0 - \phi)}{(1-\phi)}\right)$$

which eventually leads to

$$\frac{d}{d(\dot{\gamma}t)}(\phi) = -\frac{Sh}{Pe_0}3\phi_0^{2/3}\phi^{1/3}\left(S - \frac{(\phi_0 - \phi)}{(1-\phi)}\right) \tag{8}$$

This is a non-linear ODE that describes how the solids volume fraction depends on time. In this equation ϕ and Sh depend on time. The initial condition is $\phi(t\dot{\gamma} = 0) = \phi_0$. To estimate how Sh depends on Pe we use the numerical results due to Yang et al. (2011) for solid spheres in shear flow that (for $Sc = 300$) have been reprinted in Fig. 3. The following function has been fitted to the data (represented by the red line in Fig. 3):

$$Sh(Pe) = 1.3 + \alpha(2 + {}^{10}\log Pe)^{\beta} \tag{9}$$

with $\alpha = 0.0079$ and $\beta = 3.8$. The validity of Eq. (9) is largely limited to the Peclet interval shown in Fig. 3. For example, the equation does not asymptotically approach the pure diffusion limit $Sh = 1$ for $Pe \to 0$ (note that Sh is based on the sphere radius, not the diameter). Eq. (9) has been fitted to data for $Sc = 300$. Yang et al's results show that (at least for $Pe \leq 100$) Sh is virtually independent of Sc. For $Pe > 100$, there is a Schmidt number dependency. This is represented in Fig. 3 by the green curve which is a fit to Yang et al's data for $Sc = \infty$. The latter fit has the same mathematical form as Eq. (9) but now with coefficients $\alpha = 0.017$ and $\beta = 3.1$. The sensitivity of dissolution results with respect to the $Sh(Pe)$ relationship will be assessed below for one case with $Pe_0 = 800$, i.e. a case that starts in the range where the $Sh(Pe)$ correlation depends on Sc.

In order to express Eq. (8) in one dependent variable (ϕ) only, the $Sh(Pe)$ relationship (Eq. (9)) is written as $Sh(Pe) = Sh(Pe_0(\phi/\phi_0)^{2/3})$.

Numerically solving the ODE (Eq. (8)) provides time series of ϕ that can be directly compared to those coming out of the simulations. We do so in Fig. 12. Compared to the simulations, the solution of the ODE is much less steep for small times. This is no surprise as the ODE is based on a steady mass transfer coefficient where (as discussed above) initial mass transfer is highly unsteady (and much stronger due to high initial concentration gradients), an effect captured by the simulations. At later times comparing simulations and ODE solutions show an opposite difference, specifically for $\phi_0 = 0.3$ and 0.4: the slope for the ODE solution is *higher* than for the simulations. The likely reason for this is that the ODE assumes a uniform bulk concentration in the liquid (perfectly mixed liquid) and non-interacting particles. The dissolving particles are, however, in

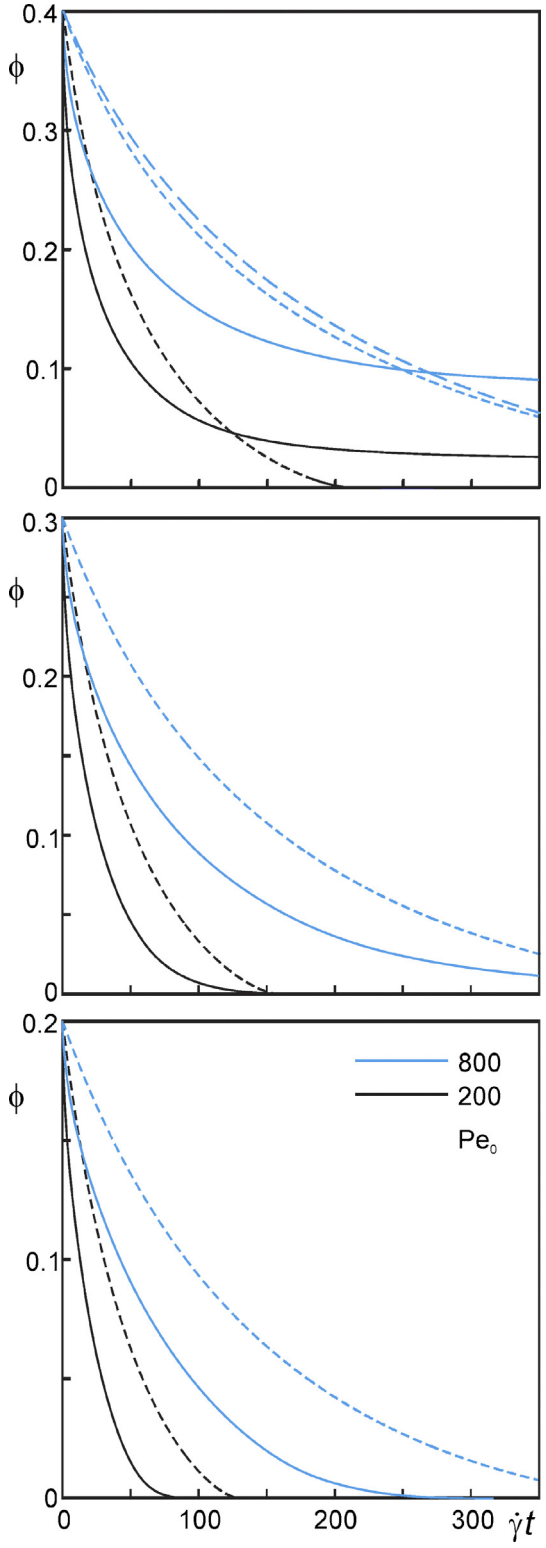

Fig. 12 – Decay of the solids volume fraction (ϕ) as a function of time as a result of dissolution. From top to bottom: $\phi_0 = 0.4$, 0.3, and 0.2. Two initial Peclet numbers and $S = 0.6$. Comparison between simulations (solid lines) and semi-analytical model predictions (dashed lines). The long-dashed line in the upper panel is based on the $Sh(Pe)$ relationship for $Sc = \infty$.

a non-uniform concentration field with concentrations surrounding the particles much higher than the volume-averaged concentration in the liquid. Furthermore, concentration fields of particles interact, and particles tend to cluster in the middle of the channel. These are all effects that slow down mass

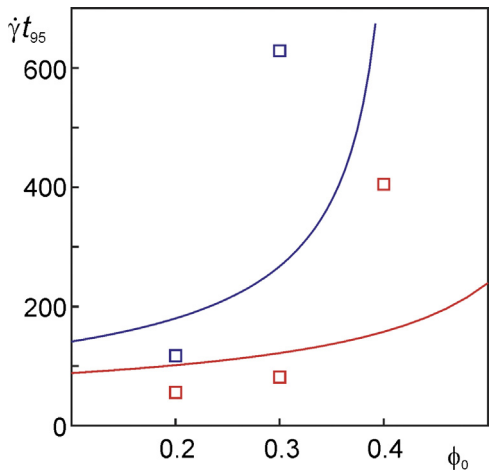

Fig. 13 – Dissolution time as a function of initial solids volume fraction. Curves: semi-analytical model (Eq. (7)); symbols: simulations. Red: $S = 0.6$; blue: $S = 0.4$. $Pe_0 = 200$.

transfer compared to the ideal case assumed in the ODE. A note of caution is appropriate here: as discussed in the section *Numerical Approach* the interaction between concentration fields of different spheres is dealt with in a rather crude way. This could imply that a more refined approach would slow down (even more) the dissolution in stages of the process where particle-concentration-fields interact strongly.

The top panel of Fig. 12 also shows – for the more relevant case with $Pe_0 = 800$ – the influence of the specifics of the $Sh(Pe)$ correlation on the modeled dissolution process: the correlation based on $Sc = \infty$ gives a slightly slower dissolution as compared to the default correlation that was based on $Sc = 300$. However, further analysis shows that the 95% dissolution time as modeled with the two different correlations is within 1.5% which is marginal in light of the model's assumptions and uncertainties.

The opposing differences between the ODE solutions (slower decay initially, faster decay later) and the simulations make it less appropriate to compare them in terms of 95% dissolution times. Differences would compensate, thereby obscuring the (over)schematizations contained in the ODE. Still we make the comparison in Fig. 13. It shows (for one initial Peclet number $Pe_0 = 200$) that the dissolution times as predicted by the semi-analytical model follow the same trends as the simulations and have dissolutions times of the same order of magnitude. For the rest the quantitative agreement is rather poor.

7. Conclusions

Motivated by hot melt extrusion as a way to disperse (drug) material in a polymer matrix, simulations of solids dissolving in a liquid in simple shear flow have been performed. The liquid is Newtonian and the solids are spheres whose radii decrease in time. Except for lubrication force modeling, the solid–liquid flow is fully resolved, i.e. the no-slip conditions at the (translating and rotating) solid sphere surfaces have been imposed explicitly. Dissolution is the result of mass being transferred from solid to liquid and the dissolved mass being transported away from the solid–liquid interface as a result of diffusion and flow.

The three main dependencies that were investigated were (in dimensionless terms) the initial solids volume fraction, the Peclet number, and the solubility. The dimensionless dissolution time ($t_{95}\dot{\gamma}$) is approximately proportional to the initial Peclet number. This means that the dimensional dissolution time is largely independent of the shear rate and therefore that (unsteady) diffusion is rate limiting for dissolution (at least in the part of the parameter space explored by the simulations). A reduction of solubility from 0.6 to 0.4 very steeply increased the dissolution time. Dense suspensions (high solids volume fraction) dissolve slower than dilute suspensions as the former give rise to higher solute concentrations in the bulk of the liquid and thus a weaker driving force for solid-to-liquid mass transfer.

We developed a semi-analytical model of the same dissolution process. It is based on a Sherwood relation that assumes steady mass transfer, and non-interacting particles. Comparison between the decay of the solids volume fraction in the "full" simulations and the semi-analytical model highlights the role of the non-idealities in the dissolution process: for short time, the unsteadiness of diffusion of solute away from the solid–liquid interfaces is important; for longer times the interaction between particles (at least in a mass-transfer sense) shows as a slow-down if dissolution in the full simulation compared to the semi-analytical model.

A major simplifying assumption in the current work is that the particles retain their spherical shape. Given the heterogeneous direct environment of each sphere (in terms of hydrodynamics as well as scalar concentration), particles will likely become non-spherical in the course of dissolving. Numerical procedures for dealing with the flow dynamics of dense suspensions of non-spherical particles are in place (Shardt and Derksen, 2012). The method for resolving mass transfer based on spherical shells around particles – as presented in the current paper – would need to be generalized to allow for body-fitted meshes around arbitrarily shaped particles. We leave this extension for future work.

References

Batchelor, G.K., 1967. Introduction to Fluid Mechanics. Cambridge University Press, Cambridge.

Bikiaris, D.N., 2011a. Solid dispersions, part I: recent evolutions and future opportunities in manufacturing methods for dissolution rate enhancement of poorly water-soluble drugs. Expert Opin. Drug Deliv. 8, 1501–1591.

Bikiaris, D.N., 2011b. Solid dispersions, part II: recent evolutions and future opportunities in manufacturing methods for dissolution rate enhancement of poorly water-soluble drugs. Expert Opin. Drug Deliv. 8, 1663–1680.

Bird, R.B., Stewart, W.E., Lightfoot, E.N., 2006. Transport Phenomena, 2nd ed. John Wiley & Sons, New York.

Chen, S., Doolen, G.D., 1998. Lattice-Boltzmann method for fluid flows. Annu. Rev. Fluid Mech. 30, 329–364.

Derksen, J.J., 2008a. Scalar mixing by granular particles. AIChE J. 54, 1741–1747.

Derksen, J.J., 2008b. Flow induced forces in sphere doublets. J. Fluid Mech. 608, 337–356.

Derksen, J.J., 2011a. Direct numerical simulations of aggregation of monosized spherical particles in homogeneous isotropic turbulence. AIChE J. 58, 2589–2600.

Derksen, J.J., 2011b. Simulations of granular bed erosion due to laminar shear flow near the critical Shields number. Phys. Fluids 23, 113303.

Derksen, J.J., Larsen, R.A., 2011. Drag and lift forces on random assemblies of wall-attached spheres in low-Reynolds number shear flow. J. Fluid Mech. 673, 548–573.

Derksen, J.J., Sundaresan, S., 2007. Direct numerical simulations of dense suspensions: wave instabilities in liquid-fluidized beds. J. Fluid Mech. 587, 303–334.

Derksen, J., Van den Akker, H.E.A., 1999. Large-eddy simulations on the flow driven by a Rushton turbine. AIChE J. 45, 209–221.
Derveaux, S., Stubbe, B., Braeckmans, K., Roelant, C., Sato, K., Demeester, J., De Smedts, S.C., 2008. Synergism between particle-based multiplexing and microfluidics technologies may bring diagnostics closer to patient. Anal. Bioanal. Chem. 391, 2453–2467.
Eggels, J.G.M., Somers, J.A., 1995. Numerical simulation of free convective flow using the lattice-Boltzmann scheme. Int. J. Heat Fluid Flow 16, 357–364.
Feng, Z-G., Michaelides, E.E., 2009. Robust treatment of no-slip boundary condition and velocity updating for the lattice-Boltzmann simulation of particulate flows. Comput. Fluids 38, 370–381.
Hartmann, H., Derksen, J.J., Van den Akker, H.E.A., 2006a. Mixing times in a turbulent stirred tank by means of LES. AIChE J. 52, 3696–3706.
Hartmann, H., Derksen, J.J., Van den Akker, H.E.A., 2006b. Numerical simulation of a dissolution process in a stirred tank reactor. Chem. Eng. Sci. 61, 3025–3032.
Jijun, F., Lili, Z., Tingting, G., Xing, T., Haibing, H., 2010. Stable nimodipine tablets with high bioavailability containing NM-SD prepared by hot-melt extrusion. Powder Technol. 204, 214–221.
Jones, W.P., Lettieri, C., Marquis, A.J., Navarro-Martinez, S., 2012. Large eddy simulation of the two-phase flow in an experimental swirl-stabilized burner. Int. J. Heat Mass Transfer 38, 145–158.
Kim, S., Karrila, S.J., 1991. Microhydrodynamics: Principles and Selected Applications. Butterworth-Heinemann, Boston.
Lakshman, J.P., Cao, Y., Kowalski, J., Serajuddin, A.T.M., 2009. Application of melt extrusion in the development of a physically and chemically stable high-energy amorphous solid dispersion of a poorly water-soluble drug. Mol. Pharm. 5, 994–1002.
Luan, Y.T., Chyou, Y.P., Wang, T., 2013. Numerical analysis of gasification performance via finite-rate model in a cross-type two-stage gasifier. Int. J. Heat Mass Transfer 57, 558–566.
Nguyen, N-Q., Ladd, A.J.C., 2002. Lubrication corrections for lattice-Boltzmann simulations of particle suspensions. Phys. Rev. E 66, 046708.
Ranz, W.E., Marshall, W.R., 1952. Evaporation from drops. Chem. Eng. Prog. 48, 142–180.
Shardt, O., Derksen, J.J., 2012. Direct simulations of dense suspensions of non-spherical particles. Int. J. Multiph. Flow 47, 25–36.
Somers, J.A., 1993. Direct simulation of fluid flow with cellular automata and the lattice-Boltzmann equation. Appl. Sci. Res. 51, 127–133.
Succi, S., 2001. The Lattice Boltzmann Equation for Fluid Dynamics and Beyond. Clarendon Press, Oxford.
Sweby, P.K., 1984. High resolution schemes using flux limiters for hyperbolic conservation laws. SIAM J. Numer. Anal. 21, 995–1011.
Ten Cate, A., Derksen, J.J., Portela, L.M., Van den Akker, H.E.A., 2004. Fully resolved simulations of monodisperse spheres in forced isotropic turbulence. J. Fluid Mech. 519, 233–271.
Ten Cate, A., Nieuwstad, C.H., Derksen, J.J., Van den Akker, H.E.A., 2002. PIV experiments and lattice-Boltzmann simulations on a single sphere settling under gravity. Phys. Fluids 14, 4012–4025.
Wang, Y., Hutter, K., 2001. Comparison of numerical methods with respect to convectively dominated problems. Int. J. Numer. Methods Fluids 37, 721–745.
Whitaker, S., 1972. Forced convection heat transfer correlations for flow in pipes, past flat plates, single cylinders, single spheres, and for flow in packed beds and tube bundles. AIChE J. 18, 361–371.
Yamamoto, Y., Potthoff, M., Tanaka, T., Kajishima, T., Tsuji, Y., 2001. Large-eddy simulation of turbulent gas-particle flow in a vertical channel: effect of considering inter-particle collisions. J. Fluid Mech. 442, 303–334.
Yang, C., Zhang, J., Koch, D.L., Yin, X., 2011. Mass/heat transfer from a neutrally buoyant sphere in simple shear flow at finite Reynolds and Peclet numbers. AIChE J. 57, 1419–1433.
Yang, M., Wang, P., Huang, C.Y., Ku, M.S., Liu, H., Gogos, C., 2010. Solid dispersion of acetaminophen and poly(ethylene oxide) prepared by hot-melt mixing. Int. J. Pharm. 395, 53–61.